

# Cross-section measurements for $^{58,60,61}\text{Ni}(n, \alpha)^{55,57,58}\text{Fe}$ reactions in the 4.50 – 5.50 MeV neutron energy region\*

Haoyu Jiang(江浩雨)<sup>1</sup> Zengqi Cui(崔增琪)<sup>1</sup> Yiwei Hu(胡益伟)<sup>1</sup> Jie Liu(刘杰)<sup>1</sup> Jinxiang Chen(陈金象)<sup>1</sup>  
Guohui Zhang(张国辉)<sup>1;1)</sup> Yu. M. Gledenov<sup>2</sup> E. Sansarbayar<sup>2</sup> G. Khuukhenkhuu<sup>3</sup> L. Krupa<sup>4,5</sup> I. Chuprakov<sup>2</sup>

<sup>1</sup>State Key Laboratory of Nuclear Physics and Technology, Institute of Heavy Ion Physics, Peking University, Beijing 100871, China

<sup>2</sup>Frank Laboratory of Neutron Physics, Joint Institute for Nuclear Research, Dubna 141980, Russia

<sup>3</sup>Nuclear Research Centre, National University of Mongolia, Ulaanbaatar 210646, Mongolia

<sup>4</sup>Flerov Laboratory of Nuclear Reactions, Joint Institute for Nuclear Research, Dubna 141980, Russia

<sup>5</sup>Institute of Experimental and Applied Physics, Czech Technical University in Prague, Horská 3a/22, Prague 2 12800, Czech Republic

**Abstract:** The cross sections at 5 energy points of the  $^{58}\text{Ni}(n, \alpha)^{55}\text{Fe}$  reaction were measured in the  $4.50 \text{ MeV} \leq E_n \leq 5.50 \text{ MeV}$  region while those for the  $^{60}\text{Ni}(n, \alpha)^{57}\text{Fe}$  and  $^{61}\text{Ni}(n, \alpha)^{58}\text{Fe}$  reactions were measured at  $E_n = 5.00$  and  $5.50 \text{ MeV}$  using the 4.5 MV Van de Graaff accelerator at Peking University. A gridded twin ionization chamber (GIC) was used as the detector, and enriched  $^{58}\text{Ni}$ ,  $^{60}\text{Ni}$ , and  $^{61}\text{Ni}$  foil samples were prepared and mounted at the sample changer of the GIC. Three highly enriched  $^{238}\text{U}_3\text{O}_8$  samples inside the GIC were used to determine the relative and absolute neutron fluxes. The neutron energy spectra were obtained through unfolding the pulse height spectra measured by the EJ-309 liquid scintillator. The interference from the low-energy neutrons and impurities in the samples has been corrected. The present data of the  $^{60}\text{Ni}(n, \alpha)^{57}\text{Fe}$  reaction are the first measurement results below 6.0 MeV, and those of the  $^{61}\text{Ni}(n, \alpha)^{58}\text{Fe}$  reactions are the first measurement results in the MeV region. The present results have been compared with existing measurements, evaluations, and TALYS-1.9 calculations.

**Keywords:**  $^{58,60,61}\text{Ni}(n, \alpha)^{55,57,58}\text{Fe}$  reactions, cross sections, GIC

**DOI:** 10.1088/1674-1137/abadf2

## 1 Introduction

Nickel is widely used for making stainless steel and other corrosion-resistant alloys which play an important role in the construction of nuclear reactors and accelerators. The  $^{58}\text{Ni}$ ,  $^{60}\text{Ni}$ , and  $^{61}\text{Ni}$  contents in natural nickel are 68.0769%, 26.2231%, and 1.1399%, respectively [1]. Research into the  $(n, \alpha)$  reactions is important in nuclear engineering applications, because neutron-induced helium production would lead to helium accumulation and cause serious radiation damage to the materials. Besides, measurements of these cross sections could enhance our understanding of nuclear structure and nuclear reaction mechanisms. For example, the cross section of the  $^{58}\text{Ni}(n, \alpha)^{55}\text{Fe}$  reaction would enable one to derive the level structure of the residual nucleus,  $^{55}\text{Fe}$  [2].

For the cross sections of the  $^{58}\text{Ni}(n, \alpha)^{55}\text{Fe}$  ( $Q = 2.899 \text{ MeV}$ ) reaction, existing measurement results are abund-

ant because the activation method is available for this reaction. In the 4.50 – 5.50 MeV neutron energy region, six measurements [2–7] could be found in the EXFOR library [8], but there are noticeable discrepancies among these measurements. For example, the cross section of the  $^{58}\text{Ni}(n, \alpha)^{55}\text{Fe}$  reaction measured by Gledenov (1997, 5.00 – 7.00 MeV) [6] is  $\sim 2$  times higher than that obtained by Goverdovskiy (1992, 5.12 MeV) [4]. Besides, the coefficient of variation among different evaluations, including the ENDF/B-VIII.0 [9], ENDF/B-VII.1 [10], JENDL-4.0u+ [11], JEFF-3.3 [12], ROSFOND-2010 [13], and CENDL-3.1 [14] libraries, is 14.92% in the  $4.50 \text{ MeV} \leq E_n \leq 5.50 \text{ MeV}$  region [15].

For the cross sections of the  $^{60}\text{Ni}(n, \alpha)^{57}\text{Fe}$  ( $Q = 1.355 \text{ MeV}$ ) and  $^{61}\text{Ni}(n, \alpha)^{58}\text{Fe}$  ( $Q = 3.580 \text{ MeV}$ ) reactions, because the residual nuclei ( $^{57}\text{Fe}$  and  $^{58}\text{Fe}$ ) of these two reactions are stable, the activation method is unavailable for measurement. For the cross sections of the  $^{60}\text{Ni}(n, \alpha)^{57}\text{Fe}$

Received 5 June 2020, Published online 19 August 2020

\* Supported by the National Natural Science Foundation of China (11775006) and China Nuclear Data Center and the Science and Technology on Nuclear Data Laboratory

1) E-mail: guohuizhang@pku.edu.cn

©2020 Chinese Physical Society and the Institute of High Energy Physics of the Chinese Academy of Sciences and the Institute of Modern Physics of the Chinese Academy of Sciences and IOP Publishing Ltd

reactions, there is only one measurement (Khromyleva (2018, 6.00 – 7.15 MeV) [16]) in the EXFOR library [8]. For the  $^{61}\text{Ni}(n, \alpha)^{58}\text{Fe}$  reaction, there is no data in the entire neutron-energy region except for several results around  $E_n = 0.0253$  eV [8]. In the  $5.00 \text{ MeV} \leq E_n \leq 5.50 \text{ MeV}$  region, the coefficients of variation among different evaluations are 36.43% and 46.85% for the  $^{60}\text{Ni}(n, \alpha)^{57}\text{Fe}$  and  $^{61}\text{Ni}(n, \alpha)^{58}\text{Fe}$  reactions, respectively [9–14].

Accurate measurements of the cross sections of the  $^{58}\text{Ni}(n, \alpha)^{55}\text{Fe}$ ,  $^{60}\text{Ni}(n, \alpha)^{57}\text{Fe}$ , and  $^{61}\text{Ni}(n, \alpha)^{58}\text{Fe}$  reactions are required. In the present work, the cross sections of the  $^{58}\text{Ni}(n, \alpha)^{55}\text{Fe}$  reaction were measured at the  $E_n = 4.50$ , 4.75, 5.00, 5.25, and 5.50 MeV energy points and those of the  $^{60}\text{Ni}(n, \alpha)^{57}\text{Fe}$  and  $^{61}\text{Ni}(n, \alpha)^{58}\text{Fe}$  reactions were obtained at the  $E_n = 5.00$  and 5.50 MeV energy points. The present data for the  $^{60}\text{Ni}(n, \alpha)^{57}\text{Fe}$  reaction are the first results of measurements below 6.0 MeV and those of the

$^{61}\text{Ni}(n, \alpha)^{58}\text{Fe}$  reactions are the first results of measurement in the MeV region. The details of the experiments are illustrated in Sect. 2, the data processing and the results are presented in Sect. 3 and Sect. 4, respectively, and the conclusion is drawn in Sect. 5.

## 2 Details of experiments

The experiments were performed based on the 4.5-MV Van de Graaff accelerator at Peking University, China. As shown in Fig. 1, the experimental apparatus consists of three main parts: the neutron source, the grid-twin ionization chamber (GIC) as the charged particle detector (with samples inside), and the scintillator detector for neutron energy spectrum measurement. The symmetric double sections of the GIC were defined as side 01 and side 02, respectively.

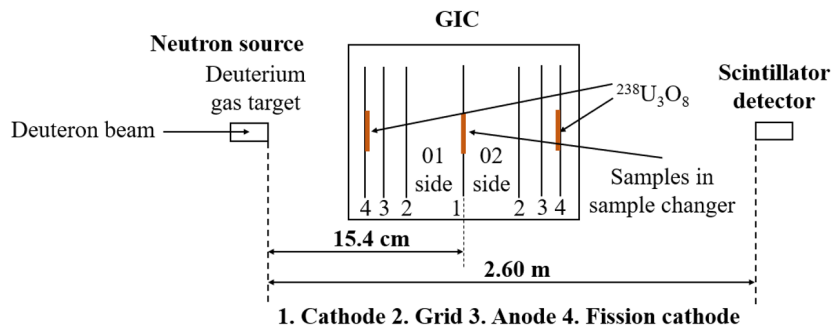


Fig. 1. (color online) Schematic drawing of the experimental apparatus.

### 2.1 Neutron source

Measurements were performed based on the 4.5-MV Van de Graaff accelerator at Peking University. The quasi mono-energetic neutrons were generated by the  $^2\text{H}(d, n)^3\text{He}$  reaction using the energetic deuteron beam from the accelerator to bombard a deuterium gas target 2.0 cm in length under a pressure of 3.0 atm. The deuterium gas target was separated from the vacuum tube of the accelerator by a 5.0  $\mu\text{m}$ -thick molybdenum foil sample. The energy range of the incident deuteron was set to 2.091 – 2.868 MeV for the neutrons to be generated with the kinetic energy range of 4.50 – 5.50 MeV and an energy spread ( $1\sigma$ ) of 0.14 – 0.19 MeV [17]. The deuteron beam current was  $\sim 2.0 \mu\text{A}$  throughout the measurement.

### 2.2 Samples

A sample changer with five sample positions was set at the common cathode of the GIC, and back-to-back double samples were placed at each of them as presented

in Table 1. The sample changer could be rotated with a rotating a knob below the GIC without opening it. The samples used in the present measurements were as follows: a) the back-to-back compound  $\alpha$  sources at sample position No.1 ( $^{234}\text{U}$ , 4.775 MeV;  $^{239}\text{Pu}$ , 5.155 MeV;  $^{238}\text{Pu}$ , 5.499 MeV;  $^{244}\text{Cm}$ , 5.805 MeV) were used to calibrate the detection system [18]; b) to monitor the neutron flux, three highly enriched (99.999%)  $^{238}\text{U}_3\text{O}_8$  samples were prepared, and their nucleus number and unevenness were determined using the  $\alpha$  spectrum measured by the GIC. Details of the method can be found in Ref. [19]. A  $^{238}\text{U}_3\text{O}_8$  sample 43.0 mm in diameter, 62.1% in unevenness, and  $600.8 \mu\text{g}/\text{cm}^2$  in average thickness at the No.2 sample position was used to determine the absolute neutron flux. The other two  $^{238}\text{U}_3\text{O}_8$  samples were glued onto the fission cathodes of the 01 and 02 sides to determine the relative neutron flux, respectively. Their diameters were 45.0 mm and 43.0 mm, unevennesses were 61.6% and 63.3%, and average thicknesses were  $604.6 \mu\text{g}/\text{cm}^2$  and  $557.5 \mu\text{g}/\text{cm}^2$ , respectively. c) Two  $^{58}\text{Ni}$  samples at the No.3 sample position, and one  $^{60}\text{Ni}$  sample and one

Table 1. Sample positions of the sample changer.

sample position	sample(01 side)	sample(02 side)	purpose
No.1	$\alpha$ source	$\alpha$ source	calibrating the detection system
No.2	$^{238}\text{U}$	Ta	measuring the absolute neutron flux
No.3	$^{58}\text{Ni}\#I$	$^{58}\text{Ni}\#II$	measuring the foreground of the $^{58}\text{Ni}(n, \alpha)^{55}\text{Fe}$ reaction
No.4	$^{61}\text{Ni}$	$^{60}\text{Ni}$	measuring the foreground of the $^{60,61}\text{Ni}(n, \alpha)^{57,58}\text{Fe}$ reactions
No.5	Ta	Ta	measuring the background of the $^{58,60,61}\text{Ni}(n, \alpha)^{55,57,58}\text{Fe}$ reactions

Table 2. Description of the Ni samples.

samples	isotopic enrichment (%)	thickness/( $\mu\text{g}/\text{cm}^2$ )	diameter/mm	preparation method
$^{58}\text{Ni}\#I^a$	99.84	601.3	46.0	rolling
$^{58}\text{Ni}\#II^a$	99.84	579.4	42.0	rolling
$^{60}\text{Ni}^b$	99.65	570.4	46.0	rolling
$^{61}\text{Ni}^c$	91.50	332.4	43.5	vacuum evaporation

<sup>a</sup> Impurities:  $^{60}\text{Ni}$  (0.15%),  $^{61}\text{Ni}$  (< 0.01%),  $^{62}\text{Ni}$  (0.01%),  $^{64}\text{Ni}$  (< 0.01%); <sup>b</sup> Impurities:  $^{58}\text{Ni}$  (0.29%),  $^{61}\text{Ni}$  (0.03%),  $^{62}\text{Ni}$  (0.03%),  $^{64}\text{Ni}$  (< 0.008%); <sup>c</sup> Impurities:  $^{58}\text{Ni}$  (2.85%),  $^{60}\text{Ni}$  (3.8%),  $^{62}\text{Ni}$  (1.65%),  $^{64}\text{Ni}$  (0.2%).

$^{61}\text{Ni}$  sample at the No.4 sample position were used to measure the foreground events, the data of which are listed in Table 2. The number of Ni atoms in the samples was determined by weighing the samples. Each Ni sample was prepared on a 0.1 mm thick tantalum backing with a diameter of 48.0 mm, as shown in Fig. 2; d) the back-to-back 0.1 mm thick tantalum backings at the No.5 position, which were 48.0 mm in diameter, were used to measure the background events.

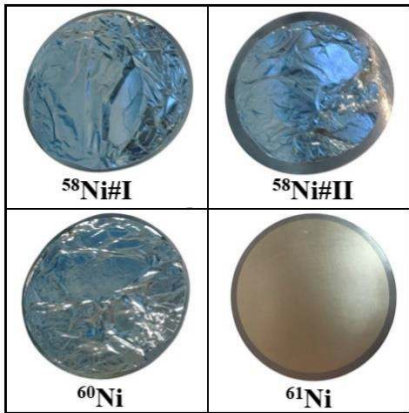


Fig. 2. (color online) Pictures of the Ni samples.

The nucleus-number uncertainty was 1.0% for the  $^{58}\text{Ni}\#I$  and  $^{61}\text{Ni}$  samples, and 5.0% for the  $^{58}\text{Ni}\#II$  and  $^{60}\text{Ni}$  samples. Although two  $^{58}\text{Ni}$  samples were used for the measurements, the  $^{58}\text{Ni}\#II$  sample had a fairly large nucleus-number uncertainty because a small section was broken during operations. Therefore, the data obtained from the two  $^{58}\text{Ni}$  samples were processed individually and the cross sections obtained for the  $^{58}\text{Ni}\#II$  sample were used to check those obtained for the  $^{58}\text{Ni}\#I$  sample. The corrections for impurity interference are detailed in

### Sect. 3.5.

## 2.3 Charged particle detector (GIC)

Comparing with our group's previous work [20], a new GIC with symmetric double sections was made and installed whose structure and electronics are shown in Fig. 3. The old GIC has been in use for ~ 20 years, and has several shortcomings, such as gas leakage at the valve and signal instability when high voltages are applied to the electrodes. The structure of the new GIC is similar to that of the old one but it has better gas tightness and low signal noise at high voltages. Besides, the new GIC has two fission cathodes (each with the capacity for a  $^{238}\text{U}$  sample) to monitor the relative neutron flux, while the old GIC had only one.

The GIC has seven electrodes: a common-cathode, two grids, two anodes, and two shields. In the present work, to monitor the relative neutron flux, two  $^{238}\text{U}_3\text{O}_8$  samples were glued onto each shield, respectively. As such, the two shields would be used as the fission cathodes of the fission chambers. The distance was 6.1 cm from the cathode to the grid, 1.4 cm from the grid to the anode, 1.0 cm from the anode to the fission cathode, and 15.4 cm from the cathode to the front surface of the neutron source. Because there is only one foil each for the  $^{60}\text{Ni}$  and  $^{61}\text{Ni}$  samples, the GIC would be rotated by 180° during the experiment to measure the forward (0° – 180°) and the backward (90° – 180°) cross sections of the  $(n, \alpha)$  reaction. To obtain higher fission tallies, only the signal of the fission cathode near the neutron source was used. For sides 01 and 02, the signals from the cathode and anode were recorded by a PDA14 waveform digitizer that was activated by the trigger control unit. The trigger control unit would produce the external trigger, which was generated by the coincidence of the cathode and the an-

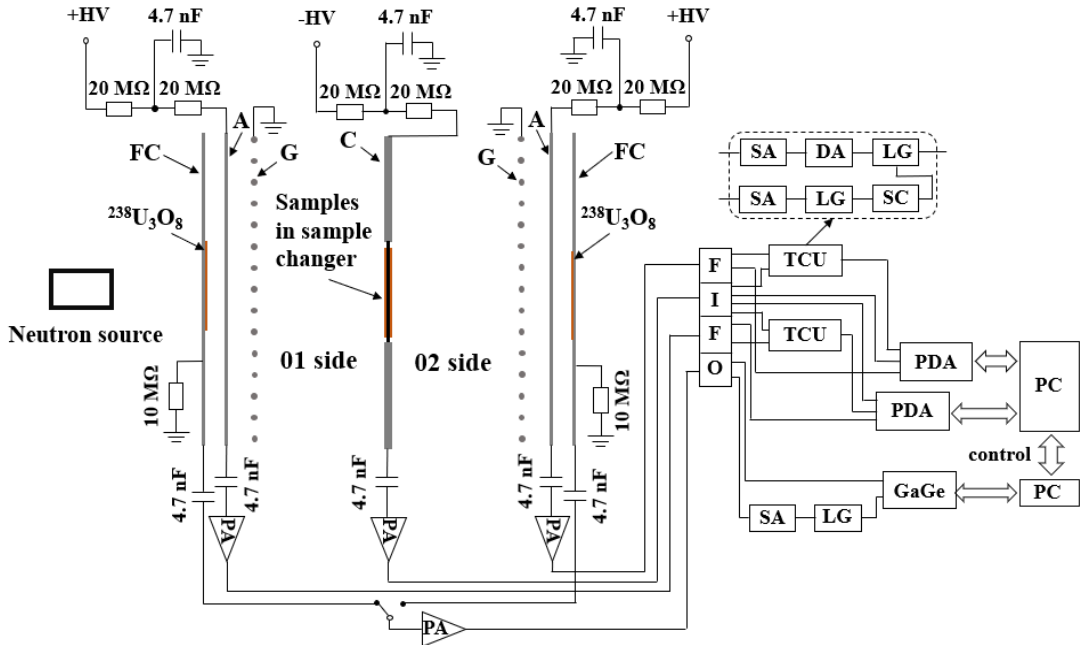


Fig. 3. (color online) The structure and the electronics of the GIC: FC, fission cathode; A, anode; G, grid; C, cathode; FIFO, fan in-fan out (CAEN N625); PA, charge sensitive preamplifier (MESYTEC MPR-1); TCU, trigger control unit; SA, signal amplifier (ORTEC 572A); DA, delay amplifier (ORTEC 427A); LG, linear gate (ORTEC 542); SC, single channel analyzer (ORTEC 551); PDA, Signatec PDA14 waveform digitizer; GaGe, GaGe OVE-832-007 high resolution PCIe digitizer.

ode signals. The trigger control unit effectively improved the anti-noise and anti-background performance of the GIC. The signal from the fission cathode was recorded by a GaGe OVE-832-007 high-resolution PCIe digitizer.

The GIC's working gas was Xe + 8.5% H<sub>2</sub> and the pressure was 0.855 atm so that the  $\alpha$ -particles could be stopped before they reached the grids. The high voltages applied to the cathodes and anodes were -1200 and 600 V (the grid electrodes were grounded), which allowed for all the electrons from the ionization tracks to be collected.

With the GIC, information on the energy and angular distribution of the detected charged particle is obtained using the cathode and anode signal amplitudes. If a charged particle is emitted from the sample on the cathode and is stopped by the work gas before it reaches the grid, the cathode signal  $V_c$  and the anode signal  $V_a$  can be represented by [21]

$$V_c = G_c E \left( 1 - \frac{\bar{X}}{d} \cos \theta \right) \quad (1)$$

and

$$V_a = G_a E \left( 1 - \delta \frac{\bar{X}}{d} \cos \theta \right) \approx G_a E, \quad (2)$$

where  $G_c$  and  $G_a$  respectively are the ratio constants of the cathode and anode that could be determined via energy calibration;  $E$  is the energy of the emitted charged particle;  $d$  is the distance between the cathode and the grid;  $\bar{X}$  is the distance from the beginning to the center of

gravity of the ionization trace; and  $\delta$  is the grid-inefficiency of the GIC. According to the theoretical calculations, in this work, the grid-inefficiency was 0.0121, which is quite low, meaning that the influence of the grid-inefficiency in the present work was negligible. The charged particle can be identified by determining the valid area in the cathode-anode two-dimensional spectrum, because according to Eqs. (1) and (2), different charged particles with the same energy and emitting angle would induce anode and cathode signals with different amplitudes due to their different ionization traces.

#### 2.4 Scintillator detector

An EJ-309 liquid scintillator detector was used to obtain the neutron spectrum by unfolding the measured pulse-height spectra [22]. The axis of the scintillator detector was along the normal line of the electrodes of the ionization chamber and the 0° direction of the deuteron beam line. The distance from the entrance surface of the scintillator detector to the front surface of the neutron source was 2.60 m.

#### 2.5 Experimental steps

For each neutron energy point, measurements were performed with the sample sequentially at the No.1, No.2, No.3, No.4, and No.5 sample positions then the GIC was rotated by 180° and measurements were performed at the No.5, No.4, No.3, No.2, and No.1 sample positions. The total neutron beam duration was  $\sim 70$  h.

During the experiment, the fission tallies obtained from the  $^{238}\text{U}_3\text{O}_8$  sample glued onto the fission cathode near the neutron source were used to monitor the relative neutron flux, and the ratio of the fission count during the foreground measurement to that during the background measurement was approximately 1:1 – 2:1. The scintillator detector would run for  $\sim 15.0$  min every hour to obtain the neutron spectrum.

### 3 Data processing

First, the compound  $\alpha$  sources were used for energy calibration and to determine the valid area of  $\alpha$  events. Second, the fission tallies from the  $^{238}\text{U}_3\text{O}_8$  samples were calculated to determine the absolute and relative neutron flux. Third, the net  $\alpha$  events from the  $^{58}\text{Ni}(n, \alpha)^{55}\text{Fe}$ ,  $^{60}\text{Ni}(n, \alpha)^{57}\text{Fe}$  and  $^{61}\text{Ni}(n, \alpha)^{58}\text{Fe}$  reactions were obtained in the valid area after the subtraction of the background, and the detection efficiency of  $\alpha$  events was calculated. Fourth, the  $\alpha$  and fission events induced by the low-energy neutrons were corrected. Fifth, the  $\alpha$  events from the impurity isotopes were corrected. Finally, the cross sections of the  $^{58}\text{Ni}(n, \alpha)^{55}\text{Fe}$ ,  $^{60}\text{Ni}(n, \alpha)^{57}\text{Fe}$ , and  $^{61}\text{Ni}(n, \alpha)^{58}\text{Fe}$  reactions were obtained, and the spread of neutron energy was unfolded into a specific energy using the iterative method.

#### 3.1 Calibration of the detection system using the compound $\alpha$ sources

The energy response of the detection system was calibrated using the compound  $\alpha$  sources. The energy of each channel could be calibrated using the four  $\alpha$  energy groups, as shown in Fig. 4. According to Eqs. (1) and (2), for the  $\alpha$  particles, if we let the emitting angles equal  $0^\circ$  and  $90^\circ$ , respectively, the  $0^\circ$  curve and  $90^\circ$  line can be drawn in the cathode-anode two-dimensional spectrum as shown in Fig. 4, by which the valid area of  $\alpha$  events can be determined. Taking the fluctuation in energy resolution into account, the valid area is a little larger than the region between the  $0^\circ$  curve and  $90^\circ$  line as shown by the two red curves in Fig. 4.

#### 3.2 Statistics of the fission tallies

The total fission tallies from the  $^{238}\text{U}_3\text{O}_8$  sample were used to determine the absolute neutron flux. A typical anode spectrum of the fission fragments is shown in Fig. 5 as an example.

The detection efficiency ( $\varepsilon_f$ ) of the fission fragments for the absolute neutron flux measurement is (75.55 – 84.93)% in the present work. A Monte Carlo simulation was used for the threshold and self-absorption corrections. The simulation code was written using Matlab-2019a [23]. The stopping power of the fission fragments

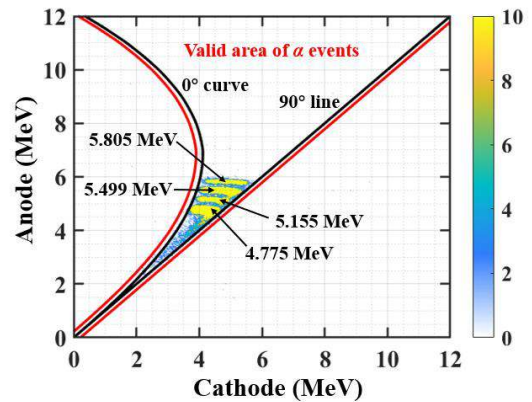


Fig. 4. (color online) The measured cathode-anode two-dimensional spectrum of the compound  $\alpha$  sources in the forward direction.

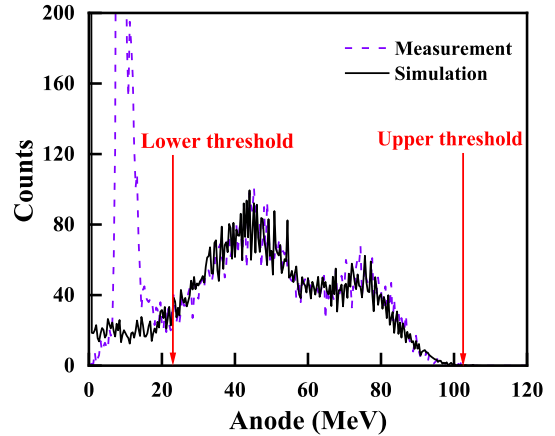


Fig. 5. (color online) The anode spectrum of the fission fragments for the absolute neutron flux measurement at  $E_n = 5.50$  MeV.

in the samples was calculated by SRIM-2013 [24], the mass distribution of the fission fragments was calculated by the GEF code [25], and the angular distributions of the fission fragments were obtained from Ref. [26]. Details of the simulation can be found in Ref. [19]. The black curve in Fig. 5 shows the simulation result for the fission fragments, which agrees well with the measurement spectrum. The shape of the simulation spectrum was almost identical at different neutron energy points, because the variation of  $E_n$  was negligible compared to the total kinetic energy (TKE) of  $^{238}\text{U}$  fission fragments ( $\sim 170$  MeV). The change of  $\varepsilon_f$  in the present results was due to the different thresholds. The threshold position was adjusted at different energy points to obtain higher fission tallies while avoiding the background. The total fission tallies could be determined by the fission tallies within the thresholds ( $N_f$ ) divided by  $\varepsilon_f$ .

As described in Sect. 2.5, the absolute neutron flux was measured as an individual experimental step, while the relative neutron flux was continuously measured for

different experimental steps. The relative neutron flux was obtained using the relative fission tallies within the thresholds of the  $^{238}\text{U}_3\text{O}_8$  sample glued onto the fission cathode for the different experimental steps. For the two fission cathodes, the thresholds were fixed, so the detection efficiency of the fission fragments can be regarded as invariant and be eliminated when calculating the relative tallies.

### 3.3 Statistics of the net $\alpha$ events

The cathode-anode two-dimensional spectra of the  $^{58}\text{Ni}(n, \alpha)^{55}\text{Fe}$ ,  $^{60}\text{Ni}(n, \alpha)^{57}\text{Fe}$ , and  $^{61}\text{Ni}(n, \alpha)^{58}\text{Fe}$  reactions were analyzed. Fig. 6(a) shows the two-dimensional spectrum for the measurement of the  $^{58}\text{Ni}(n, \alpha)^{55}\text{Fe}$  reaction in the forward direction (from the  $^{58}\text{Ni}\#1$  sample) after subtracting the background events at  $E_n = 5.50$  MeV. The background tallies were normalized using the fission tallies from the  $^{238}\text{U}_3\text{O}_8$  sample glued onto the fission cathode. The effective  $\alpha$  events could be selected in the valid

area described in Sect. 3.1. Then, the two-dimensional spectrum was projected onto the anode channel as Fig. 6(b) shows, in which the thresholds were set to separate the effective  $\alpha$  events from the background that could not be subtracted. The tally of net  $\alpha$  events within the thresholds ( $N_\alpha$ ) can be determined by

$$N_\alpha = N_\alpha^{\text{fore}} - C^{\text{f}-\text{b}} N_\alpha^{\text{back}}, \quad (3)$$

where  $N_\alpha^{\text{fore}}$  and  $N_\alpha^{\text{back}}$  are the total tallies within the thresholds of the foreground and background measurements, respectively.  $C^{\text{f}-\text{b}}$  is the background normalization coefficient, which is the ratio between the fission tallies from the  $^{238}\text{U}_3\text{O}_8$  sample glued onto the fission cathode during the foreground measurement and those during the background measurement. The detection efficiency of the  $\alpha$  particles was determined from the simulation results of the anode spectrum. Detection efficiency was related to the neutron energy and the threshold of which the details will be described in Sect. 3.4.

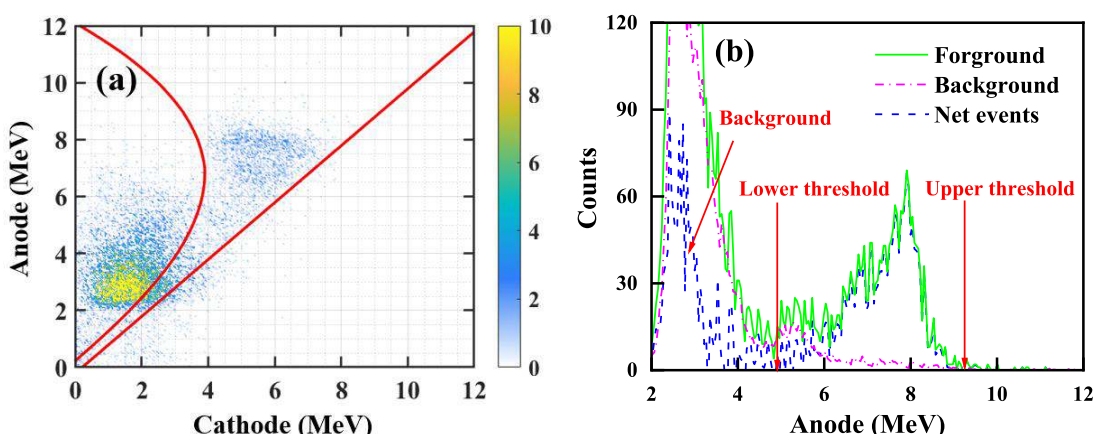


Fig. 6. (color online) (a) The cathode-anode two-dimensional spectrum after subtracting background events and (b) the anode projection spectrum of the foreground, background, and net events for the measurement of the  $^{58}\text{Ni}(n, \alpha)^{55}\text{Fe}$  reaction in the forward direction (from the  $^{58}\text{Ni}\#1$  sample) at  $E_n = 5.50$  MeV.

### 3.4 Correction of the events induced by the low-energy neutrons

The neutron spectrum at each energy point was obtained by unfolding the pulse height spectra measured by an EJ-309 liquid scintillator detector [22]. The neutron energy spectrum at  $E_n = 5.5$  MeV is shown in Fig. 7 as an example (neutrons with the energy below 1 MeV were ignored because they hardly affect the results). The energy of the neutrons is divided into two parts: the main neutron region around the peak at  $E_n = 5.50$  MeV, and the low-energy neutron region. The variation in the spectrum resulting from the difference between the positions of the scintillator detector and the GIC was corrected using the Monte Carlo method [27]. In the present work, the low-

energy neutrons account for 9.29% – 16.50% of the total, and the  $\alpha$  events and fission events they induced should be corrected.  $k_\alpha^{\text{low}}$  and  $k_f^{\text{low}}$  are defined as the proportion of  $\alpha$  events and fission events within the thresholds induced by low-energy neutrons, respectively, and they would be calculated as follows.

The angular and energy distributions of the  $\alpha$  events from the  $(n, \alpha)$  reaction will change at different neutron energy points, thus changing the detection efficiency; therefore, the anode spectra induced by the neutrons with different energies should be simulated.

For the simulation, the relative intensities of the neutrons at different energy bins were obtained from the measured neutron spectrum, the stopping power of  $\alpha$

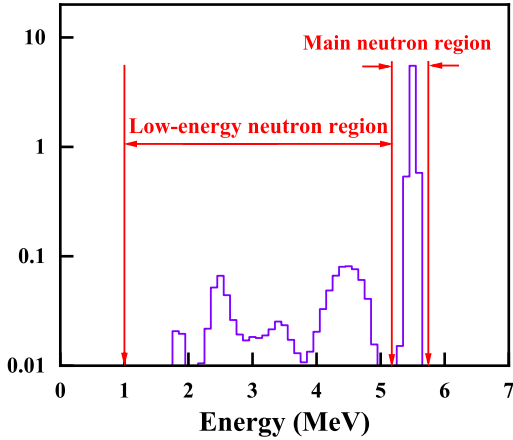


Fig. 7. (color online) Neutron spectrum at  $E_n = 5.50$  MeV (neutrons with the energy under 1 MeV were ignored).

particles in the samples was calculated using SRIM-2013 [24], the angular and energy distributions of  $\alpha$  particles were calculated using TALYS-1.9 [28] and, for the initial condition, the cross sections were obtained from the ENDF/B-VIII.0 library [9]. Because the tallies of the simulated spectrum may be systematically higher or lower than those measured, the simulated spectrum was multiplied by a factor to fit the measurements, which means that only the variation trend in the cross sections obtained from the ENDF/B-VIII.0 library was used in the present results. The detection efficiencies of  $\alpha$  events ( $\varepsilon_\alpha$ ) were obtained from the simulated spectrum. According to the simulation,  $\varepsilon_\alpha$  is 86.73% – 92.64% for the  $^{58}\text{Ni}(n, \alpha)^{55}\text{Fe}$  reaction in the  $4.50 \text{ MeV} \leq E_n \leq 5.50 \text{ MeV}$  region, 69.47% – 87.00% for the  $^{60}\text{Ni}(n, \alpha)^{57}\text{Fe}$  reaction, and 84.11% – 91.48% for the  $^{61}\text{Ni}(n, \alpha)^{58}\text{Fe}$  reaction in the  $5.00 \text{ MeV} \leq E_n \leq 5.50 \text{ MeV}$  region.

Because the cross sections were not measured for low neutron energy in the present work, it is necessary to use the evaluation cross sections to calculate the final results. To estimate the uncertainty of the evaluation cross sections, the ENDF/B-VII.1 library was used, and the final result was recalculated. Then, the difference between the new result and the previous result was regarded as the uncertainty.

As an example, Fig. 8 shows the  $\alpha$  events of the  $^{58}\text{Ni}(n, \alpha)^{55}\text{Fe}$  reaction (in the forward direction at  $E_n = 5.50$  MeV) induced by the total neutrons, main neutrons, low-energy neutrons, and the neutrons with 5.50 MeV of specific energy as “Simulation (total neutrons),” “Simulation (main neutrons),” “Simulation (low-energy neutrons),” and “Simulation ([5.50 MeV] neutrons),” respectively. Using the simulated spectra of “Simulation (low-energy neutrons)” and “Simulation (total neutrons),” the proportion of  $\alpha$  events within the thresholds induced by the low-energy neutrons ( $k_\alpha^{\text{low}}$ ) could be determined. The values of  $k_\alpha^{\text{low}}$  are 2.93% – 5.25%, 0.22% – 1.35%, and 2.96% – 4.44% for the  $^{58}\text{Ni}(n, \alpha)^{55}\text{Fe}$ ,  $^{60}\text{Ni}(n, \alpha)^{57}\text{Fe}$ ,

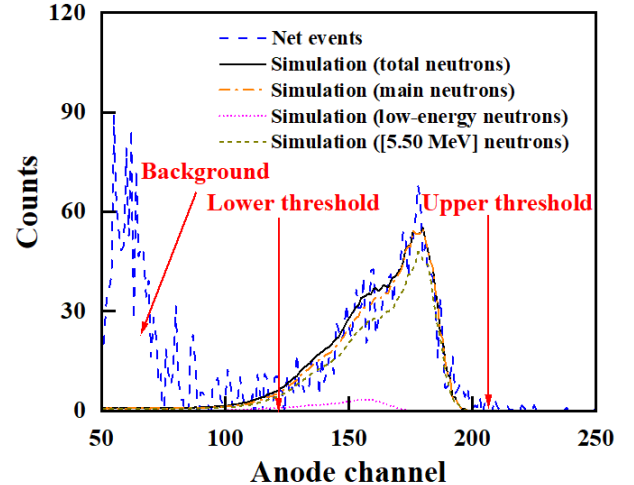


Fig. 8. (color online) The measured and simulated anode projection spectrum for the measurement of the  $^{58}\text{Ni}(n, \alpha)^{55}\text{Fe}$  reaction in the forward direction (from the  $^{58}\text{Ni}$  sample) at  $E_n = 5.50$  MeV. The simulated  $\alpha$  events were induced by the neutrons in different energy regions.

and  $^{61}\text{Ni}(n, \alpha)^{58}\text{Fe}$  reactions, respectively.

As described in Sect. 3.2, the detection efficiency of the fission events could be regarded as invariant with the change of neutron energy when the thresholds were fixed; it can then be eliminated when the proportion of fission events induced by the neutrons with different energies is calculated. Therefore, the proportion of the fission events within the thresholds induced by the low-energy neutrons ( $k_f^{\text{low}}$ ) could be determined using the standard cross section of the  $^{238}\text{U}(n, f)$  reaction [29] and the measured neutron spectrum. According to calculation,  $k_f^{\text{low}}$  is 9.41% – 16.32% at different neutron energy points.

The correction coefficient of the events induced by low-energy neutrons ( $\rho^{\text{low}}$ ) was introduced by

$$\rho^{\text{low}} = \frac{1 - k_\alpha^{\text{low}}}{1 - k_f^{\text{low}}} \quad (4)$$

The values of  $\rho^{\text{low}}$  are 1.064 – 1.132, 1.125 – 1.164, and 1.090 – 1.127 for the  $^{58}\text{Ni}(n, \alpha)^{55}\text{Fe}$ ,  $^{60}\text{Ni}(n, \alpha)^{57}\text{Fe}$ , and  $^{61}\text{Ni}(n, \alpha)^{58}\text{Fe}$  reactions, respectively. The values of  $\rho^{\text{low}}$  are greater than 1, because the low-energy neutrons would have a stronger influence on fission events than on  $\alpha$  events.

### 3.5 Correction the $\alpha$ events from the impurity isotopes

As shown in Table 2, in addition to the main isotopes in the samples there are some impurity isotopes, including  $^{58}\text{Ni}$ ,  $^{60}\text{Ni}$ ,  $^{61}\text{Ni}$ ,  $^{62}\text{Ni}$ , and  $^{64}\text{Ni}$ . The  $\alpha$  events arising from the  $^{62}\text{Ni}$  and  $^{64}\text{Ni}$  impurity isotopes hardly affect the results because the cross sections of the  $(n, \alpha)$  reactions of these two isotopes were smaller than those of other isotopes by two orders of magnitude [15]. Therefore, only

the influences of the  $^{58}\text{Ni}$ ,  $^{60}\text{Ni}$ , and  $^{61}\text{Ni}$  isotopes were taken into consideration.

The interference arising from the impurities was negligible in the  $^{58}\text{Ni}(n, \alpha)^{55}\text{Fe}$  reaction measurements because the cross sections of the  $(n, \alpha)$  reactions of the  $^{60}\text{Ni}$  and  $^{61}\text{Ni}$  impurity isotopes were fairly small compared with those in the  $^{58}\text{Ni}(n, \alpha)^{55}\text{Fe}$  reaction, and the purity of the  $^{58}\text{Ni}$  sample was very high (99.84%). In the  $^{60}\text{Ni}(n, \alpha)^{57}\text{Fe}$  and  $^{61}\text{Ni}(n, \alpha)^{58}\text{Fe}$  reaction measurements, the interference from the impurities in the samples was non-negligible because the cross sections of the two reactions were approximately 70% – 90% lower than those of the  $^{58}\text{Ni}(n, \alpha)^{55}\text{Fe}$  reaction and  $^{58}\text{Ni}$  was the main impurity isotope in the  $^{60}\text{Ni}$  and  $^{61}\text{Ni}$  samples.

To correct the interference of the impurity isotopes, the anode spectrum contributed by different isotopic compositions was simulated according to their proportions presented in Table 1. A typical example is shown in Fig. 9. The conditions for the simulation were similar to those described in Sect. 3.3 but the cross sections of the  $(n, \alpha)$  from the impurity isotopes were obtained from the present results: in the measurement of the  $^{58}\text{Ni}(n, \alpha)^{55}\text{Fe}$  reaction, the interference from the impurities was negligible and consequently the cross sections of the  $^{58}\text{Ni}(n, \alpha)^{55}\text{Fe}$  reaction could be obtained without correcting for the impurity isotopes; then, for the measurement of the  $^{60}\text{Ni}(n, \alpha)^{57}\text{Fe}$  reaction, the interference was mainly from the  $^{58}\text{Ni}(n, \alpha)^{55}\text{Fe}$  reaction, the cross sections of which already had been obtained; lastly, for the measurement of the  $^{61}\text{Ni}(n, \alpha)^{58}\text{Fe}$  reaction, the interference was mainly from the  $^{58}\text{Ni}(n, \alpha)^{55}\text{Fe}$  and  $^{60}\text{Ni}(n, \alpha)^{57}\text{Fe}$  reactions, the cross sections of which had also been obtained already.

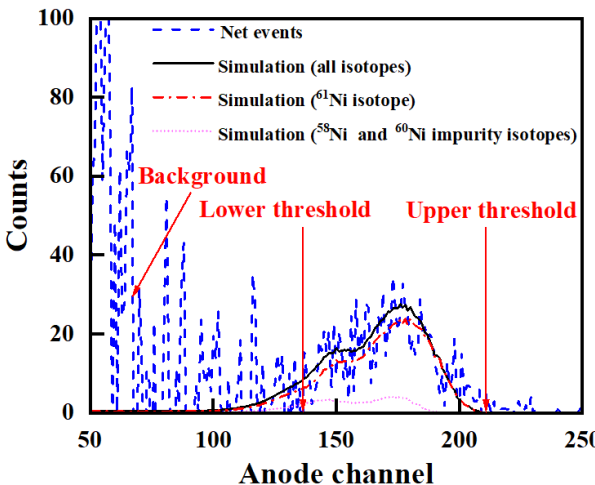


Fig. 9. (color online) The measured and simulated anode projection spectrum for the measurement of the  $^{61}\text{Ni}(n, \alpha)^{55}\text{Fe}$  reaction in the forward direction at  $E_n = 5.50$  MeV. The simulated  $\alpha$  events were from all isotopes in the  $^{61}\text{Ni}$  sample, including the  $^{61}\text{Ni}$  isotope and the  $^{58}\text{Ni}$  and  $^{60}\text{Ni}$  impurity isotopes.

The tallies of the  $\alpha$  events from different isotopes could be determined from the simulated results. The proportion of  $\alpha$  events arising from the impurity isotope ( $\beta^{\text{impurity}}$ ) could be determined using the ratio between the simulated tallies within the thresholds of the impurity isotopes and those of all isotopes.  $\beta^{\text{impurity}}$  is  $\sim 0\%$  for the  $^{58}\text{Ni}(n, \alpha)^{55}\text{Fe}$  reaction,  $0.89\% - 1.07\%$  for the  $^{60}\text{Ni}(n, \alpha)^{57}\text{Fe}$  reaction, and  $11.69\% - 12.95\%$  for the  $^{61}\text{Ni}(n, \alpha)^{58}\text{Fe}$  reaction.

### 3.6 Calculation of the cross sections

Either the forward or backward cross sections ( $\sigma_\alpha$ ) of the  $(n, \alpha)$  reactions can be calculated by

$$\sigma_\alpha = \sigma_f \cdot \frac{N_U \cdot N_\alpha \cdot \varepsilon_f \cdot \rho^{\text{low}} \cdot (1 - \beta^{\text{impurity}})}{N_{\text{Ni}} \cdot N_f \cdot \varepsilon_\alpha \cdot G \cdot C_{\text{f-fission}}} \cdot R^{\text{unfolding}}, \quad (5)$$

where  $\sigma_f$  is the standard cross section of the  $^{238}\text{U}(n, f)$  reaction, and the values of  $\sigma_f$  in the present results are 0.5592, 0.5579, 0.5483, 0.5517, and 0.5482 b at  $E_n = 4.50, 4.75, 5.00, 5.25$ , and  $5.50$  MeV, respectively [29].  $N_U$  and  $N_{\text{Ni}}$  are the numbers of  $^{238}\text{U}$  and  $^{58, 60, 61}\text{Ni}$  nuclei in the samples, respectively.  $N_\alpha$  and  $N_f$  are the tallies of the net  $\alpha$  events and fission events described in Sects. 3.3 and 3.2, respectively.  $\varepsilon_f$  and  $\varepsilon_\alpha$  are the detection efficiencies for the fission fragments and  $\alpha$  particles at the specific neutron energy described in Sect. 3.2 and 3.3, respectively.  $\rho^{\text{low}}$  is the correction coefficient of the events induced by the low-energy neutrons described in Sect. 3.5.  $\beta^{\text{impurity}}$  is the proportion of  $\alpha$  events arising from the impurity isotope described in Sect. 3.5.  $G = 0.9890 - 1.003$  is the ratio between the average neutron flux in the area of the nickel sample and that of the  $^{238}\text{U}_3\text{O}_8$  sample in the sample changer, and  $G$  is obtained by the Monte Carlo method ( $G$  is introduced because there is a slight difference between the diameters of the two samples).  $C_{\text{f-fission}}$  is the ratio between the fission tallies from the  $^{238}\text{U}_3\text{O}_8$  sample glued onto the fission cathode during the foreground measurement and those obtained during the absolute neutron flux measurement.  $R^{\text{unfolding}}$  is the unfolding coefficient that is explained as follows.

According to the measured neutron spectrum shown in Fig. 7, in the main neutron region, the width of the neutron peak is non-negligible and the corresponding uncertainty of  $E_n$  is 2.5% – 4.2% in the  $4.50 \text{ MeV} \leq E_n \leq 5.50 \text{ MeV}$  region. The spread of neutron energy could be unfolded using the iterative method.  $k_\alpha^{\bar{E}_n}$  and  $k_f^{\bar{E}_n}$ , which are the ratios between the tallies of the  $\alpha$  and fission events within the thresholds induced by the neutrons with the specific energy  $\bar{E}_n$  and those induced by the main neutrons that were determined for unfolding the neutron spectrum.

$k_\alpha^{\bar{E}_n}$  can be determined using the simulation method. As shown in Fig. 8, the  $\alpha$  events induced by main neut-

rons and the neutrons with the specific energy  $\bar{E}_n$  can be determined using the simulated tallies of “Simulation (main neutrons)” and “Simulation ([5.50 MeV] neutrons).” The conditions for simulation were the same as those described in Sect. 3.3 except for the cross section of the  $(n, \alpha)$  reaction. The forward or backward cross section of the  $(n, \alpha)$  reaction was obtained from the last iteration using Eq. (3). In the main neutron region, the neutron energies are very close and the excitation functions of the  $(n, \alpha)$  reactions are smooth; therefore, the cross section can be obtained from the measured results using the linear interpolation or extrapolation method.  $k_f^{\bar{E}_n}$  could be determined using the standard cross section of the  $^{238}\text{U}(n, f)$  reactions [29] and the measured neutron spectrum.

Next, the unfolding coefficient  $R^{\text{unfolding}}$  was calculated by

$$R^{\text{unfolding}} = \frac{k_{\alpha}^{\bar{E}_n}}{k_f^{\bar{E}_n}}. \quad (6)$$

Then, the new cross section  $\sigma_{\alpha}$  would be calculated using Eq. (5). This deconvolution process was iterated until the variation of the cross section was less than 0.1% (usually 10 times).  $R^{\text{unfolding}}$  was set to 1 as the initial value. In the present work, the final value of  $R^{\text{unfolding}}$  is 0.9705–1.018, which would slightly correct the original results by -2.95%–1.80%. The value of  $R^{\text{unfolding}}$  is mainly affected by the average neutron energy in the main neutron region. If the average neutron energy is smaller than the specific energy  $\bar{E}_n$ ,  $R^{\text{unfolding}}$  would be greater than 1; otherwise, it would be less than 1. The unfolding method

could decrease the uncertainty of  $E_n$  from 2.5%–4.2% to 1.4%–1.5%, and the final uncertainty of  $E_n$  is contributed by the energy resolution of the scintillator detector.

## 4 Results

### 4.1 Measured results

The forward and backward cross sections of the  $^{58}\text{Ni}(n, \alpha)^{55}\text{Fe}$ ,  $^{60}\text{Ni}(n, \alpha)^{57}\text{Fe}$ , and  $^{61}\text{Ni}(n, \alpha)^{58}\text{Fe}$  reactions can be calculated using Eq. (5). The sources of uncertainty and their magnitudes are presented in Table 3. The total  $(n, \alpha)$  cross section could be obtained by adding the forward cross section to the backward. Further, the forward/backward ratios in the laboratory reference system could be obtained by division. The results are shown in Tables 4–6 and Figs. 10–12 (results of the  $^{58}\text{Ni}(n, \alpha)^{55}\text{Fe}$  reaction were obtained from the  $^{58}\text{Ni}\#I$  sample).

As described in Sect. 2.2, the present cross sections of the  $^{58}\text{Ni}(n, \alpha)^{55}\text{Fe}$  reaction were obtained from the  $^{58}\text{Ni}\#I$  sample, and they were checked using the results obtained from the  $^{58}\text{Ni}\#II$  sample, as Fig. 13 shows. The results obtained from the two samples agreed, thus verifying the reliability of the measurement results.

### 4.2 Theoretical calculation using TALYS-1.9

TALYS-1.9 [28] was used to calculate the cross sections of the  $^{58}\text{Ni}(n, \alpha)^{55}\text{Fe}$ ,  $^{60}\text{Ni}(n, \alpha)^{57}\text{Fe}$ , and  $^{61}\text{Ni}(n, \alpha)^{58}\text{Fe}$  reactions. To attain better agreement with the present results, several input parameters, including those of the optic, level density, and stripping models, were adjusted from the default input values, as listed in Table 7

Table 3. Sources of the uncertainty and their magnitudes.

source	magnitude (%)		
	$^{58}\text{Ni}(n, \alpha)^{55}\text{Fe}$	$^{60}\text{Ni}(n, \alpha)^{57}\text{Fe}$	$^{61}\text{Ni}(n, \alpha)^{58}\text{Fe}$
$N_U$	1.0 <sup>a,b</sup>	1.0 <sup>a,b</sup>	1.0 <sup>a,b</sup>
$N_{\text{Ni}}$	1.0 <sup>a,b</sup>	5.0 <sup>a,b</sup>	1.0 <sup>a,b</sup>
$\sigma_f$	0.6–0.7 <sup>a,b</sup>	0.6–0.7 <sup>a,b</sup>	0.6–0.7 <sup>a,b</sup>
$N_a$	2.9–4.4 <sup>a</sup> , 2.7–5.0 <sup>b</sup>	8.0–11.6 <sup>a</sup> , 13.2–18.5 <sup>b</sup>	6.4–7.0 <sup>a</sup> , 8.3–8.5 <sup>b</sup>
$N_f$	1.0–1.1 <sup>a,b</sup>	1.0–1.1 <sup>a,b</sup>	1.0–1.1 <sup>a,b</sup>
$\rho^{\text{low}}$	1.4–1.7 <sup>a</sup> , 1.0–2.1 <sup>b</sup>	1.4–1.6 <sup>a</sup> , 1.5–1.6 <sup>b</sup>	1.4–1.7 <sup>a</sup> , 1.5–1.7 <sup>b</sup>
$\varepsilon_f$	1.9–3.1 <sup>a,b</sup>	2.1–3.1 <sup>a,b</sup>	2.1–3.1 <sup>a,b</sup>
$\varepsilon_{\alpha}$	1.8–3.2 <sup>a</sup> , 2.2–3.3 <sup>b</sup>	3.3–6.2 <sup>a</sup> , 6.5–7.6 <sup>b</sup>	2.2–4.0 <sup>a</sup> , 2.1–3.5 <sup>b</sup>
$G$	<0.5 <sup>a,b</sup>	<0.5 <sup>a,b</sup>	<0.5 <sup>a,b</sup>
$\beta^{\text{impurity}}$	—	<0.1 <sup>a,b</sup>	1.8–2.0 <sup>a</sup> , 1.8–1.9 <sup>b</sup>
$R^{\text{unfolding}}$	1.0–2.1 <sup>a</sup> , 1.0–2.7 <sup>b</sup>	2.0–3.7 <sup>a</sup> , 1.0–4.6 <sup>b</sup>	0.3–1.1 <sup>a</sup> , 0.5–1.1 <sup>b</sup>
$E_n$ (later error after the unfolding process)	1.4–1.5 <sup>a,b</sup>	1.4–1.5 <sup>a,b</sup>	1.4–1.5 <sup>a,b</sup>
$\sigma_{\alpha}$	5.2–6.6 <sup>a</sup> , 5.3–7.6 <sup>b</sup> , 5.2–7.0 <sup>c</sup>	11.6–12.8 <sup>a</sup> , 15.7–20.4 <sup>b</sup> , 13.9–15.0 <sup>c</sup>	8.6–8.7 <sup>a</sup> , 9.8–10.2 <sup>b</sup> , 9.0–9.4 <sup>c</sup>

<sup>a</sup> For the forward cross section; <sup>b</sup> For the backward cross section; <sup>c</sup> For the total cross section (forward cross section + backward cross section).

Table 4. Measured  $^{58}\text{Ni}(n, \alpha)^{55}\text{Fe}$  cross sections and forward/backward ratios in the laboratory reference system (results were obtained from the  $^{58}\text{Ni}$ # sample) compared with TALYS-1.9 calculations using the adjusted input parameters.

$E_n/\text{MeV}$	cross section /mb		forward/backward ratio	
	measurement	calculation	measurement	calculation
$4.50 \pm 0.07$	$25.7 \pm 1.3$	24.6	$0.96 \pm 0.07$	1.05
$4.75 \pm 0.07$	$28.7 \pm 2.0$	30.7	$1.03 \pm 0.10$	1.05
$5.00 \pm 0.07$	$37.2 \pm 2.2$	36.8	$1.03 \pm 0.09$	1.05
$5.25 \pm 0.08$	$44.6 \pm 2.7$	42.9	$1.05 \pm 0.09$	1.05
$5.50 \pm 0.08$	$51.7 \pm 3.0$	48.7	$1.04 \pm 0.08$	1.04

Table 5. Measured  $^{60}\text{Ni}(n, \alpha)^{57}\text{Fe}$  cross sections and forward/backward ratios in the laboratory reference system compared with TALYS-1.9 calculations using the adjusted input parameters.

$E_n/\text{MeV}$	cross section /mb		forward/backward ratio	
	measurement	calculation	measurement	calculation
$5.00 \pm 0.07$	$4.22 \pm 0.63$	4.03	$1.31 \pm 0.31$	1.06
$5.50 \pm 0.08$	$7.87 \pm 1.09$	8.10	$1.32 \pm 0.27$	1.05

Table 6. Measured  $^{61}\text{Ni}(n, \alpha)^{58}\text{Fe}$  cross sections and forward/backward ratios in the laboratory reference system compared with TALYS-1.9 calculations using the adjusted input parameters.

$E_n/\text{MeV}$	cross section /mb		forward/backward ratio	
	measurement	calculation	measurement	calculation
$5.00 \pm 0.07$	$9.40 \pm 0.84$	9.36	$1.04 \pm 0.13$	1.05
$5.50 \pm 0.08$	$11.9 \pm 1.1$	12.0	$1.00 \pm 0.13$	1.04

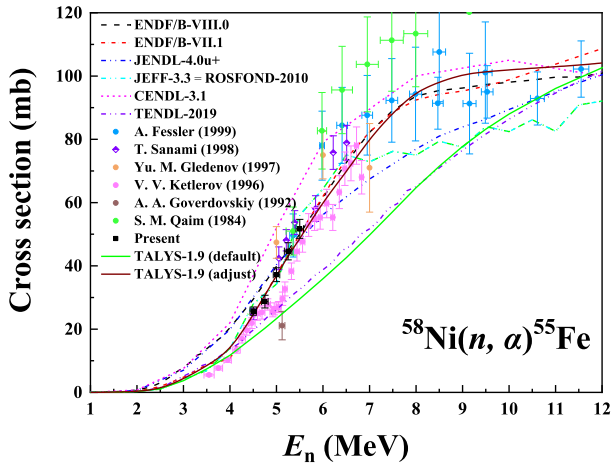


Fig. 10. (color online) The present  $^{58}\text{Ni}(n, \alpha)^{55}\text{Fe}$  cross sections (obtained from the  $^{58}\text{Ni}$ # sample) compared with existing measurements and evaluations and TALYS-1.9 calculations [8, 15, 28, 30].

(parameters of the stripping model mainly affect the results for  $E_n > 10.0$  MeV). The calculated cross sections and forward/backward ratios agree well with the measured results, as presented in Tables 4 – 6 and Figs. 10 – 12. With the adjusted parameters, the calculated cross sections of other major reaction channels, including the

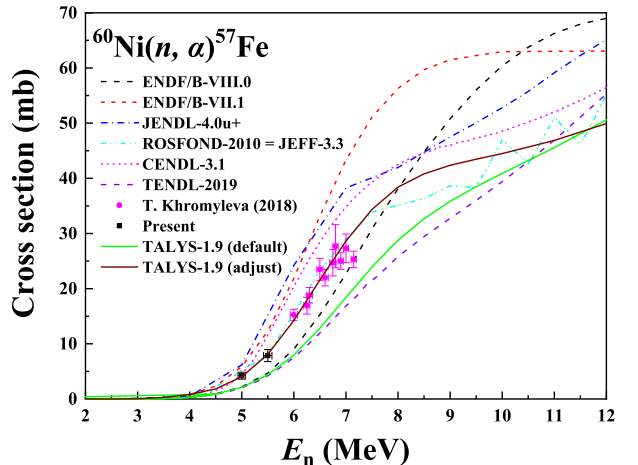


Fig. 11. (color online) The present  $^{60}\text{Ni}(n, \alpha)^{57}\text{Fe}$  cross sections compared with existing measurements, evaluations and TALYS-1.9 calculations [8, 15, 28, 30].

$(n, \text{tot})$ ,  $(n, \text{el})$ ,  $(n, n')$ , and  $(n, p)$  reactions, and the angular distributions of elastic scattering have been checked. The calculated results of these reactions also agree well with most existing measurements and evaluations, thus verifying the reliability of the adjusted parameters.

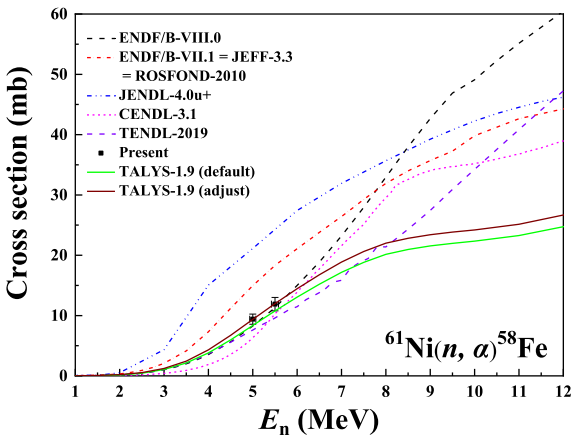


Fig. 12. (color online) The present  $^{61}\text{Ni}(n, \alpha)^{58}\text{Fe}$  cross sections compared with existing measurements and evaluations and TALYS-1.9 calculations [8, 15, 28, 30].

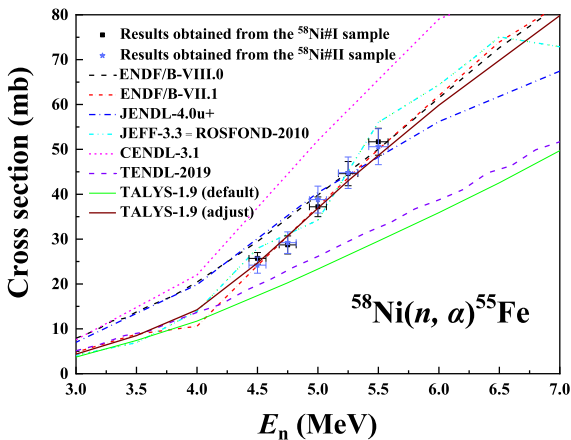


Fig. 13. (color online) The present  $^{58}\text{Ni}(n, \alpha)^{55}\text{Fe}$  cross sections obtained from the  $^{58}\text{Ni}\#I$  and  $^{58}\text{Ni}\#II$  samples compared with evaluations and TALYS-1.9 calculations [15, 28, 30].

Table 7. Adjusted input parameters of TALYS-1.9.

$^{58}\text{Ni}(n, \alpha)^{55}\text{Fe}$		$^{60}\text{Ni}(n, \alpha)^{57}\text{Fe}$	
keyword	parameter	keyword	parameter
rvadjust <sup>a</sup>	p 1.03	rvadjust <sup>a</sup>	p 1.14
rvadjust <sup>a</sup>	a 0.92	rvadjust <sup>a</sup>	a 1.091
rwadjust <sup>a</sup>	a 1.58	aadjust <sup>b</sup>	28 60 1.14
tljadjust <sup>a</sup>	a 0.50 1		
tljadjust <sup>a</sup>	a 1.50 1		
tljadjust <sup>a</sup>	a 3.00 2		
tljadjust <sup>a</sup>	a 2.02 3	$^{61}\text{Ni}(n, \alpha)^{58}\text{Fe}$	
aadjust <sup>b</sup>	26 55 0.90	keyword	parameter
tadjust <sup>b</sup>	26 55 0.95	rvadjust <sup>a</sup>	p 1.12
cstrip <sup>c</sup>	a 0.80	rvadjust <sup>a</sup>	a 1.02

<sup>a</sup> parameters of the optic model [28]; <sup>b</sup> parameters of the level density model [28]; <sup>c</sup> parameters of the stripping model [28].

### 4.3 Comparison of the results with existing measurements and evaluations

The present cross sections were compared with existing measurement data obtained from the EXFOR library [8] and evaluations obtained from the ENDF/B-VIII.0 [9], ENDF/B-VII.1 [10], JENDL-4.0u+ [11], JEFF-3.3 [12], ROSFOND-2010 [13], CENDL-3.1 [14], and TENDL-2019 [30] libraries:

1) For the  $^{58}\text{Ni}(n, \alpha)^{55}\text{Fe}$  reaction, the present cross sections in the  $4.50 \text{ MeV} \leq E_n \leq 5.50 \text{ MeV}$  region agree well with the measurement data of Fessler (1999,  $5.36 - 19.4 \text{ MeV}$ ) [7], T. Sanami (1998,  $4.51 - 6.51 \text{ MeV}$ ) [2], S. M. Qaim (1984,  $5.36 - 9.49 \text{ MeV}$ ) [3], and the ENDF/B-VII.1 evaluation [10]. Besides, the excitation function calculated using TALYS-1.9 with the adjusted parameters also accords with the ENDF/B-VII.1 evaluation [10].

The present cross sections are 21.6% lower than those in the measurement data of Gledenov (1997,  $5.00 - 7.00 \text{ MeV}$ ) [6] and 79.1% higher than those of Goverdovskiy (1992,  $5.12 \text{ MeV}$ ) [4] in the  $4.50 \text{ MeV} \leq E_n \leq 5.50 \text{ MeV}$  region. Compared with other measurement data in this neutron energy region, the Gledenov [6] and Goverdovskiy [4] results respectively have the highest and the lowest values. Uncertainties in their results are greater than 10%, while those in the present results are less than 7%. The V. V. Ketlerov (1996,  $3.55 - 6.83 \text{ MeV}$ ) [5] measurement data suggest that the excitation function has a “valley structure” around  $E_n = 4.92 \text{ MeV}$ . However, the present results and none of the evaluations show this structure [9 - 14, 30].

2) For the  $^{60}\text{Ni}(n, \alpha)^{57}\text{Fe}$  reaction, there is only one measurement (Khromyleva (2018,  $6.00 - 7.15 \text{ MeV}$ ) [16] in the MeV region, which consistent with our measurement results. The present cross sections agree well with the data from the JEFF-3.3 (= ROSFOND-2010) library [12, 13]. The excitation function calculated using TALYS-1.9 with the adjusted parameters accords with both measurements and the JEFF-3.3 (= ROSFOND-2010) library [12, 13].

3) For the  $^{61}\text{Ni}(n, \alpha)^{58}\text{Fe}$  reaction, there is no measurement in the MeV region and there is a significant deviation among different evaluations. Compared with various other evaluations, the present results better agree with the ENDF/B-VIII.0 library [9]. The excitation function calculated using TALYS-1.9 with the adjusted parameters is close to the ENDF/B-VIII.0 library for  $E_n < 6.0 \text{ MeV}$  [9] and the TENDL-2019 library for  $E_n > 6.0 \text{ MeV}$  [30].

As presented in Tables 4, 5, and 6 the nearly symmetrical distributions for the forward and backward directions of the outgoing alpha-particles mean that the com-

ound mechanism is predominant for the  $^{58}\text{Ni}(n, \alpha)^{55}\text{Fe}$  and  $^{61}\text{Ni}(n, \alpha)^{58}\text{Fe}$  reactions. However, in the case of the  $^{60}\text{Ni}(n, \alpha)^{57}\text{Fe}$  reaction, a slight non-statistical effect may be available.

#### 4.4 Future plan

Above the  $E_n = 5.50$  MeV region, the cross sections of the  $^{58}\text{Ni}(n, \alpha)^{55}\text{Fe}$ ,  $^{60}\text{Ni}(n, \alpha)^{57}\text{Fe}$ , and  $^{61}\text{Ni}(n, \alpha)^{58}\text{Fe}$  reactions noticeably grow correspondingly with the increase in neutron energy. The cross sections of the three reactions in the  $8.50 \text{ MeV} \leq E_n \leq 10.50 \text{ MeV}$  region are approximately 2 – 10 times larger than those in the  $4.50 \text{ MeV} \leq E_n \leq 5.50 \text{ MeV}$  region [9]. However, in the  $8.50 \text{ MeV} \leq E_n \leq 10.50 \text{ MeV}$  region, the existing measurement data for the  $^{58}\text{Ni}(n, \alpha)^{55}\text{Fe}$  reactions are scarce, and there is no measurement for the  $^{60}\text{Ni}(n, \alpha)^{57}\text{Fe}$  and  $^{61}\text{Ni}(n, \alpha)^{58}\text{Fe}$  reactions [8]. Further, there are significant discrepancies among different evaluations in this neutron energy region [9]. Taking these factors into consideration, measurements of the cross sections of the three reactions are planned in the  $8.50 \text{ MeV} \leq E_n \leq 10.50 \text{ MeV}$  region based on the HI-13 tandem accelerator of the China Institute of Atomic Energy (CIAE).

## 5 Conclusions

In the present work, the cross sections of the  $^{58}\text{Ni}(n, \alpha)^{55}\text{Fe}$ ,  $^{60}\text{Ni}(n, \alpha)^{57}\text{Fe}$ , and  $^{61}\text{Ni}(n, \alpha)^{58}\text{Fe}$  reactions were measured in the  $4.50 - 5.50 \text{ MeV}$  neutron-energy region using the 4.5-MV Van de Graaff accelerator, GIC detector, enriched nickel isotopic foil samples,  $^{238}\text{U}_3\text{O}_8$  samples, and the EJ-309 liquid scintillator detector. The present data of the  $^{58}\text{Ni}(n, \alpha)^{55}\text{Fe}$  reaction are consistent with the data of most measurements and the ENDF/B-VII.1 evaluation [8, 10]. The present data of the  $^{60}\text{Ni}(n, \alpha)^{57}\text{Fe}$  reaction are the first measurement results below 6.0 MeV, and those of the  $^{61}\text{Ni}(n, \alpha)^{58}\text{Fe}$  reactions are the first measurement results in the MeV region. The results calculated using TALYS-1.9 with the parameters adjusted agree well with the present data. These results would contribute significantly to clarifying the deviations and discrepancies among the measurements and evaluations to date.

*The authors are indebted to the operations crew of the 4.5-MV Van de Graaff accelerator at Peking University. Dr. Qiwen Fan from the China Institute of Atomic Energy is acknowledged and thanked for preparing the  $^{58}\text{Ni}$ ,  $^{60}\text{Ni}$ , and  $^{61}\text{Ni}$  samples.*

## References

- 1 E. M. Baum, M. C. Ernesti, H. D. Knox *et al.*, Nuclides and Isotopes. Chart of the Nuclides, 17-th Edition, KAPL, New York, 2010
- 2 T. Sanami, M. Baba, T. Kawano *et al.*, *Jour. of Nucl. Sci. and Techn.*, **35**: 851 (1998)
- 3 S. M. Qaim, R. Wolfle, M. M. Rahman *et al.*, *Nucl. Sci. Eng.*, **88**: 143 (1984)
- 4 A. A. Goverdovskiy, O. T. Grudzevich, A. V. Zelenetskiy *et al.*, *Fiz.-Energ Institut, Obninsk Reports*, No.2242(1992)
- 5 V. V. Ketlerov, A. A. Goverdovskij, V. F. Mitrofanov *et al.*, *Ser. Yadernye Konstanty*, **1**: 121 (1996)
- 6 Yu. M. Gledenov, M. V. Sedysheva, G. Khuukhenkhuu *et al.*, *Conf. on Nucl. Data for Sci. and Techn.*, Trieste, **1**: 514 (1997)
- 7 A. Fessler and S. M. Qaim, *Radiochimica Acta*, **84**: 1 (1999)
- 8 EXFOR: Experimental Nuclear Reaction Data, <https://www-nds.iaea.org/exfor/exfor.htm>
- 9 D. A. Brown, M. B. Chadwick, R. Capote *et al.*, *Nucl. Data Sheets*, **148**: 1 (2018)
- 10 M. B. Chadwick, M. Herman, P. Obložinský *et al.*, *Nucl. Data Sheets*, **112**: 2887 (2011)
- 11 K. Shibata, O. Iwamoto, T. Nakagawa *et al.*, *Nucl. Sci. Technol.*, **48**: 1 (2011)
- 12 A. J. Koning, O. Bersillon, R. A. Forrest *et al.*, *J. Korean Phys. Soc.*, **59**(2): 1057 (2011)
- 13 S. Zabrodskaya, A. Ignatyuk, V. Kosheev *et al.*, *Ser. Nucl. Const.*, **1-2**: 3 (2007)
- 14 Z. G. Ge, Z. X. Zhao, H. H. Xia *et al.*, *J. Korean Phys. Soc.*, **59**(2): 1052 (2011)
- 15 ENDF: Evaluated Nuclear Data File, <https://www-nds.iaea.org/exfor/endf.htm>
- 16 T. Khromyleva, I. Bondarenko, A. Gurbich *et al.*, *Nucl. Sci. Eng.*, **191**: 282 (2018)
- 17 G. Zhang, Yu. M. Gledenov, G. Khuukhenkhuu *et al.*, *Phys. Rev. Lett.*, **107**: 252502 (2011)
- 18 H. Bai, Z. Wang, L. Zhang *et al.*, *Appl. Radiat. Isot.*, **125**: 34 (2017)
- 19 H. Bai, H. Jiang, Y. Lu, *et al.*, *Appl. Radiat. Isot.*, **152**: 180 (2019)
- 20 H. Bai, H. Jiang, Y. Lu *et al.*, *Phys. Rev. C*, **99**: 024619 (2019)
- 21 Xuemei Zhang, Zemin Chen, Yingtang Chen, *et al.*, *Phys. Rev. C*, **61**: 054607 (2000)
- 22 H. Bai, Z. Wang, L. Zhang *et al.*, *Nucl. Instrum. Methods Phys. Res. A*, **886**: 109 (2018)
- 23 Matlab, <https://www.mathworks.cn/products/matlab.html>
- 24 J. F. Ziegler, SRIM-2013, <http://www.srim.org/#SRIM>
- 25 K.-H. Schmidt, B. Jurado, C. Amouroux *et al.*, *Nucl. Data Sheets*, **131**: 107 (2016)
- 26 A. S. Vorobyev, A. M. Gagarski, O. A. Shcherbakov *et al.*, *EPJ Web of Conferences*, **146**: 04011 (2017)
- 27 R. A. Forster, L. J. Cox, R. F. Barrett *et al.*, *Nucl. Instrum. Methods Phys. Res. B*, **213**: 82 (2004)
- 28 A. J. Koning, S. Hilaire, and M. C. Duijvestijn, TALYS-1.9, <http://www.TALYS.eu/>
- 29 Neutron Cross-section References (2015), [https://www-nds.iaea.org/standards/references/238U\\_nf\\_Reference\\_xs\\_data.txt](https://www-nds.iaea.org/standards/references/238U_nf_Reference_xs_data.txt)
- 30 A. J. Koning, D. Rochman, J. Sublet *et al.*, *Nucl. Data Sheets*, **155**: 1 (2019)